JOM, Vol. 72, No. 4, 2020
https://doi.org/10.1007/s11837-019-03974-y

Control of Porosity in Freeze Casting

S. GIL-DURAN,[1,2] D. AROLA,[3,4] and E.A. OSSA [1,5]

1.—Production Engineering Department, Universidad Eafit, Cra 49 No 7 sur 50, Medellín, Colombia. 2.—Quality and Production Engineering Department, Instituto Tecnológico Metropolitano, Medellín, Colombia. 3.—Department of Materials Science and Engineering, University of Washington, Seattle, WA, USA. 4.—Departments of Restorative Dentistry and Oral Health Sciences, School of Dentistry, University of Washington, Seattle, WA, USA. 5.—e-mail: eossa@eafit.edu.co

Many biologic structural materials have porous microstructures with a distribution and orientation of pores that are challenging to achieve using traditional methods of processing. In this investigation, numerical and experimental methods of evaluation were used to understand effects from the primary processing parameters on the temperature gradients during solidification in freeze casting of ceramics. The location and orientation of the temperature gradients were found to be highly dependent on the geometrical and thermal properties of the mold material used in processing. Furthermore, it was found that careful control of these processing variables can be used to design bioinspired porous materials with graded orientations and distributions of pores.

INTRODUCTION

Among biologic structural materials, bone is exceptional because of its ability to combine strength, stiffness and toughness with rather limited weight.[1] This is largely attributable to its hierarchical microstructure.[2] At the macroscale, bone consist of porous structures with interconnectivity, a specific aspect ratio, distribution and varying orientations depending on the particular structural requirements.[3]

In recent years, scientists have explored the adoption of different manufacturing techniques for developing synthetic materials with controlled porosity.[4–8] Among the candidates, freeze casting is a relatively new technique for developing porous materials, which allows control of the pore size and shape through proper control of specific process variables.[8–12] The porosity of materials developed by freeze casting has very characteristic microstructures, which can be qualitatively described as being lamellar, dendritic, cellular, honeycomb and/or columnar. Based on the unique qualities of structures available, this process is an excellent candidate for the manufacture of "bone-like" materials or biomaterials with controlled porosity.

The freeze-casting process involves four basic steps: (1) ceramic slurry preparation, (2) freezing of the slurry, (3) sublimation and (4) sintering. Most contributions in this area have argued that the most important step for controlling pore morphology is related to slurry preparation.[13] The slurry consists of particles suspended in a colloidal medium (fluid). While ceramics are the most commonly used particles, metallic and polymeric particles can also be employed in the process.[9] The choice of the medium and additives largely determines the resulting pore morphology.

Water-based suspensions are the most commonly studied in freeze casting, since there is a wide range of porous structures that can be achieved. The predominant pore structure obtained with water-based slurries is lamellar, with distinct plate-like morphologies. A change in suspension characteristics through additives has been shown to modify the morphology, substituting lamellar with dendritic or cellular structures.[14–16] The concentration of the particles within the slurry also has an effect on the final part. As expected, increasing concentrations lead to denser materials[17]; a linear relationship between the porosity and initial solid content of the slurry has been reported.[18,19] Another important parameter is the particle size, with more detailed structures obtained with smaller particles. During freezing, the direction[9] and rate[12,20] of freezing are important parameters to control pore morphology.

Once the freezing has been completed, the samples must be lyophilized to sublimate the frozen liquid phase. As a result, the lyophilized sample has

(Published online January 2, 2020)

a porous structure with a replica of the crystal shape formed during freezing. After sublimation, the sample is in a "green" state, where it can hold the form and shape. Nevertheless, it is not durable enough in this state for mechanical loads. The sublimation process takes place in a chamber with temperature and pressure, which are particular to each solvent. To the authors' knowledge, no studies have reported the effects of the lyophilization process variables on the pore morphology. As a final step, sintering of the cast ceramic is performed in a furnace. Depending on the sintering temperature, the material structure can undergo densification, which affects the pore morphology and distribution.[9] Thus, while the flexibility that is achieved from the range in processing variables is an advantage, it adds significant complexity to understanding the principles that govern porosity-process relationships.

As in freeze casting the pore characteristics are the result of fluid solidification, the driver of the crystal nucleation and growth during freezing is the temperature distribution within the medium. Altogether, freeze casting offers a tremendous opportunity to create synthetic materials that could lead to the development of novel structures for a wide range of applications.[21,22] Although abundant literature is available on the freeze-casting process, knowledge of the fundamental aspects of ice nucleation and growth, which are the result of atomistic events driven by thermal fluctuations, is far from complete.[23,24]

Although the freeze-casting process is customizable based on setting specific process variables, controlling the development of the pore structure during processing can be challenging.[25–27] Effects of mold design with varying contact areas within the heat sink have been studied to modify the pore structure.[28] Highly porous SiC ceramics have also been obtained by using several freezing conditions combined with finite element analysis.[29] The use of numerical simulations to predict the structures and morphologies of freeze-cast materials have been also applied to produce porous scaffolds from collagen [30] and chitosan-alginate scaffolds.[31] Thus, computer simulation is a promising route for creating complex designs with ceramic materials.

The aim of the current study is to test the following hypothesis: the porous morphologies of materials obtained by the freeze-casting process can be predicted by the temperature gradients during freezing. The objective of this work is to evaluate, by means of numerical modeling and experimentation, the effect of cooling patterns on the porous morphology of freeze-cast ceramics. Understanding how these cooling patterns can be used to control the ceramic microstructure in freeze casting will facilitate the manufacture of advanced porous bioinspired structures.

MATERIALS AND METHODS

Materials

The ceramic slurry used in this investigation was prepared using distilled water as the aqueous medium. Alumina powder ($Al_2O_3 \geq 99.999\%$) was used as the ceramic material with average particle size of 500 nm (MSESUPPLIES) at 30 wt%. Polyvinyl alcohol (341584 Aldrich, Mw 89,000–98,000) was used as an organic deflocculant at 1.4 wt.% of the alumina powder. Poly(vinyl) alcohol works as a binder, increasing the strength of the green part.[24] The zeta potential of the alumina slurry was measured as a function of pH. The pH of the samples was adjusted to different values from 2 up to 12. The zeta potential measurements were performed using Malvern Zetasize equipment at room temperature (293.15 K).

Colloidal interactions govern whether the particles in the fluid aggregate or remain separated.[32] The zeta potential characterizes the surface properties of the particles in suspension. The magnitude of this parameter is often used as a measure of the strength of the repulsive interactions between particles. Chemical and physical properties of the particle's surface and medium are affected by its adsorption of polyelectrolytes,[33] with higher adsorbed concentrations favoring stability and low adsorbed concentrations promoting flocculation. The isoelectric point, where the slurry is unstable, and the zeta potential is zero, was located at pH 2.4. Therefore, to have particles in suspension before the freezing process, the alumina slurry was kept at pH 6.0, with a zeta potential of − 20 mV.

Experimental Methods

Several ceramic materials were manufactured by freeze casting to study their porous morphology. All samples were manufactured using cylindrical molds with 40 mm inner diameter, 50 mm height and 5 mm thickness of the container mold (Fig. 1). To have extremes in thermal conduction and evaluate the effect of thermal properties of the mold on the cooling patterns of the frozen ceramic slurry, two molds were manufactured, one each using rubber (k = 1 W/m K^{-1}) and aluminum (k = 167 W/m K^{-1}). Both were prepared with the same surface finish. In all the cases the base of the mold in contact with the freezing medium was made of aluminum with a thickness of 5 mm (k = 167 W/m K^{-1}).

Approximately 40 mm of each mold was filled with the alumina slurry. The base of the molds was kept at constant temperatures of T_1 = 203.15 K, T_2 = 143.15 K or T_3 = 93.15 K to evaluate the effect of the freezing rate on the pore morphology.

After freezing, the samples were subjected to freeze drying for 12 h to allow sublimation of the ice (VirTis BenchTop 4 K, 16 mTorr at 193 K), according to.[34] Finally, sintering was performed at

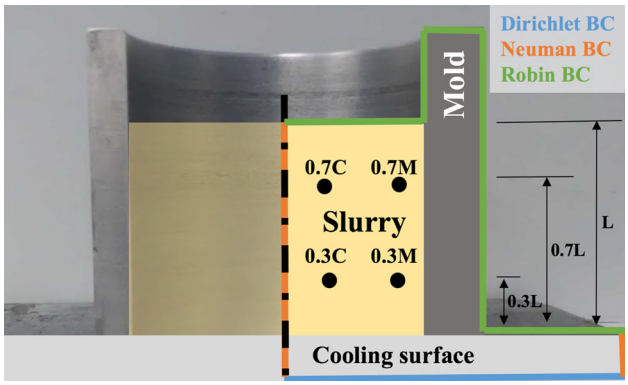

Fig. 1. Schematic diagram showing the experimental setup and boundary conditions used in the finite element modeling. The points shown in the slurry at 0.3 L and 0.7 L represent positions selected for analysis close to the axis of the slurry (C) and to the mold (M).

1773.15 K in a convective furnace (Nabertherm LHT 04/17).

To study the pore morphology and distribution within the samples, optical microscopy (Zeiss, Discovery V8) was performed in reflection mode to measure the effects of variations in the process parameters on pore morphology. Sintered samples were cut in half along the longitudinal direction using a diamond slicing disc. Pore density (λ), defined as the number of pores counted over a 1 mm distance, was measured for the manufactured samples using the magnifications necessary to easily differentiate neighbor pores (i.e., 60 $\times$). Measurements were performed at consistent and specific positions in all samples, corresponding to 0.3 l and 0.7 l of the mold height as shown in Fig. 1. A microscopic computed tomography (micro-CT) system (North Star Imaging X5000) was used to determine porous patterning at macro-levels, enabling a quantitative evaluation of distribution at the micro and macro levels. The CT parameters used for all the scans were voltage = 80 kV, current = 600 μA, geometric zoom = $\times$ 8.21, resolution = $\sim$ 35.2 μm, number of projections = 1200, frame average = 2 and frame rate = 1 fps. A phantom-like reference material was not used for calibration. The beam distortion was corrected by an offset and three gain maps of the detector in air.

Numerical Methods

Numerical modeling was performed to analyze the temperature distribution within the experimental domain corresponding to the mold and ceramic slurry. The modeling consisted of solving the heat equations with given boundary conditions. The freezing device was simplified as a cooling surface on which the mold containing the colloidal suspension was placed. A full description of the numerical model used and its validation can be found in the Electronic Supplementary Material.

The heat transfer problem for simulating freezing within the experimental cylindrical mold (Fig. 1) can be simplified as an axisymmetric problem with three domains corresponding to: (1) the cooling plate, (2) the mold material and (3) the colloidal suspension. Each domain has its own thermal properties. The boundary conditions (BCs) of the model were defined as [35]: Dirichlet boundary conditions, referring to a situation where the temperature at any surface is controlled directly. In our domain, the bottom of the experiment, which is in direct contact with the cooling elements, was set to maintain a fixed constant temperature with this BC. On the other hand, Neumann boundary conditions equal to zero model a situation where the heat flow rate is controlled. In our experiments, this condition was applied to the axisymmetric axis since the heat cannot enter or leave through that boundary. Finally, Robin boundary conditions were applied as a convective boundary condition. In our experiment, it was used to represent the movement of the air around the experiment.

The temperature evolution within the experiment is a time-dependent process, and the final gradient direction was obtained in short periods of time, obtaining the same results if the analysis was carried out after the steady state was reached. Therefore, after analysis of the final effect of the transient time-dependent part of the process on the pore formation and orientations, it was found that there were no considerable effects.

The heat equation of this problem is a parabolic partial differential equation and can be written as:

$$\frac{\partial T}{\partial t} - \alpha \nabla^2 T = 0, \tag{1}$$

where T is the temperature, t the time and α the thermal diffusivity, defined as:

$$\alpha = \frac{k}{C_p \rho}, \tag{2}$$

with k representing the thermal conductivity, C_p the specific heat capacity and ρ the mass density of the material. The thermal properties of the ceramic slurry depend on various parameters, including the thermal conductivity of the base fluid and particles, volume fraction of particles, surface area, shape of the particles and temperature of the system, among others. There are no theoretical approaches available to predict the thermal properties for the ceramic slurry.[36] Nonetheless, there are some semi-empirical correlations that can be used to estimate the thermal conductivity. The classic Maxwell model predicts the thermal conductivity of solid-liquid mixtures (K) based on the thermal conductivity of the base fluid (km), particles (kp)—assuming they are spherical—and volume fraction of ø particles according to:[37]

$$\frac{K}{km} = 1 + \frac{3\phi}{\left(\frac{kp+2km}{kp-km}\right) - \phi}. \tag{3}$$

Furthermore, the parameter $C_p\rho$ in Eq. 2 for the ceramic slurry was estimated using the approach proposed by Xuan and Roetzel [38] following the rule of mixtures. Table I summarizes the thermal properties of the materials used in the calculations.

A finite element modeling software (Freefem++; v3.57) was employed to simulate the effects of the experimental parameters on the cooling patterns in the ceramic slurry. The simulations were validated using an analytical model for special cases (see Electronic Supporting Information and Figures S1 and S2 for details). The parameters specified in the model include the convective coefficient, thermal conductivity of the materials, diameter and thickness of the mold, and temperature at the base of the mold in contact with the cooling plate (e.g., freezing temperature). To compare the effects of varying the control parameters, a pair of points was chosen at two different radial distances from the axis of symmetry, which were located at 0.3 L and 0.7 L of the total height of the ceramic slurry (Fig. 1). One set of points was positioned 5 mm from the axis of symmetry (e.g., 0.3 C and 0.7 C), and the second was 5 mm away from the mold (e.g., 0.3 M and 0.7 M). The difference in temperature between the two points (i.e., $T_M - T_C$) was calculated to evaluate temperature differences at critical zones in the sample domain. A difference in temperature between the points close to zero shows that there were no temperature differences between the *center* and mold. Alternatively, there were positive or negative differences in temperature.

RESULTS AND DISCUSSION

Figure 2a shows the microstructural pattern resulting from the freezing process for a sample that was revealed by micro-CT evaluation. In addition, at higher magnification Fig. 2b shows the lamellar distribution of the pores obtained. A comparison of the samples produced by freezing within the two different mold materials is shown in Fig. 3. Specifically, the samples developed in the aluminum mold are shown in Fig. 3a–c for the mold base temperatures of 203 K, 143 K and 103 K, respectively. Similarly, the samples developed in the rubber mold at these three temperatures are shown in Fig. 3d–f, respectively. This general comparison shows that each sample displayed a unique freezing pattern that depended on the cooling temperature and mold material. Nevertheless, the mold material played a substantial role in the freezing patterns as evident from comparing Fig. 3a–c with d–f.

Well-defined lamellar macro-pores were observed in all of the samples developed (see Fig. 2b). However, they exhibited different particle-frozen front interactions throughout the sample as a consequence of the different freezing temperatures, leading to particular pore morphologies and orientations.

Figure 4 shows the variation in the number of pores per millimeter as a function of freezing temperature and position within the samples. Results for the samples fabricated using the aluminum and rubber molds are shown in Fig. 4a and b, respectively. Interestingly, for samples prepared using the aluminum mold there were no significant differences in pore distribution when comparing the two slurry positions (e.g., 0.3 L and 0.7 L), as shown in Fig. 4a. However, the cooling temperature does have an important effect on pore density; smaller pores resulted when the mold temperature driving the freezing process was reduced. On the other hand, for samples prepared using the rubber mold, there were significant differences in the pore density as a function of distance from the cooling plate and in terms of the freezing temperature, as shown in Fig. 4b.

Figure 5 shows the effect of varying mold geometries on the FEA results. For instance, as shown in Fig. 5a, increasing the mold wall thickness from 4 mm to 45 mm results in a reduction of the temperature difference in the slurry domain between the center and mold region at the two points of evaluation (0.3 L and 0.7 L). Furthermore, there is a mold thickness value (15 mm) that causes a remarkable change in the slope of the curve. From that point on, increasing the mold wall thickness

Table I. Thermal properties of the ceramic slurry with 30% solid content, aluminum mold and rubber

	Thermal conductivity (K) (W/(m K))	Specific heat capacity (C_p) (J/(g °C))	Mass density (ρ) (g/cc)
Aluminum	210	0.9	2.69
Rubber	0.15	0.44	0.95
Ceramic slurry (30% solid content)	1.856 *	3.945**	
Aluminum oxide	26	0.9	3.8
Water	0.6	4.17	1

*Calculated using Eq. 3**Calculated using Xuan & Roetzel's [31] model

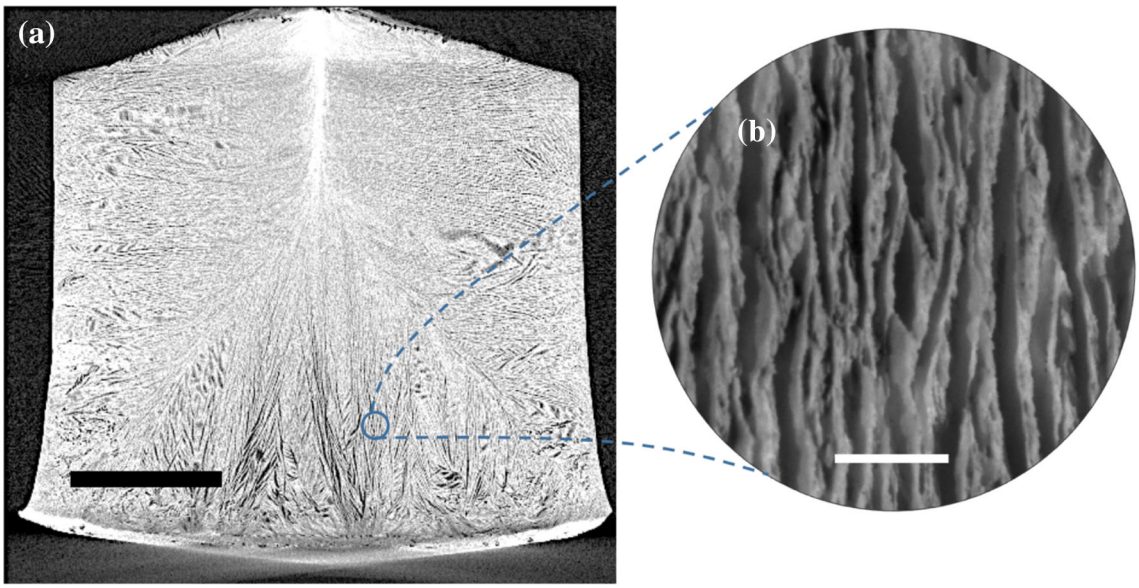

Fig. 2. Freeze-cast sample manufactured using the aluminum mold at cooling temperature of 203 K. (a) Micro-CT image; the scale bar represents 10 mm. (b) Optical microscopy image showing the lamellar pore morphology; the scale bar represents 500 μm.

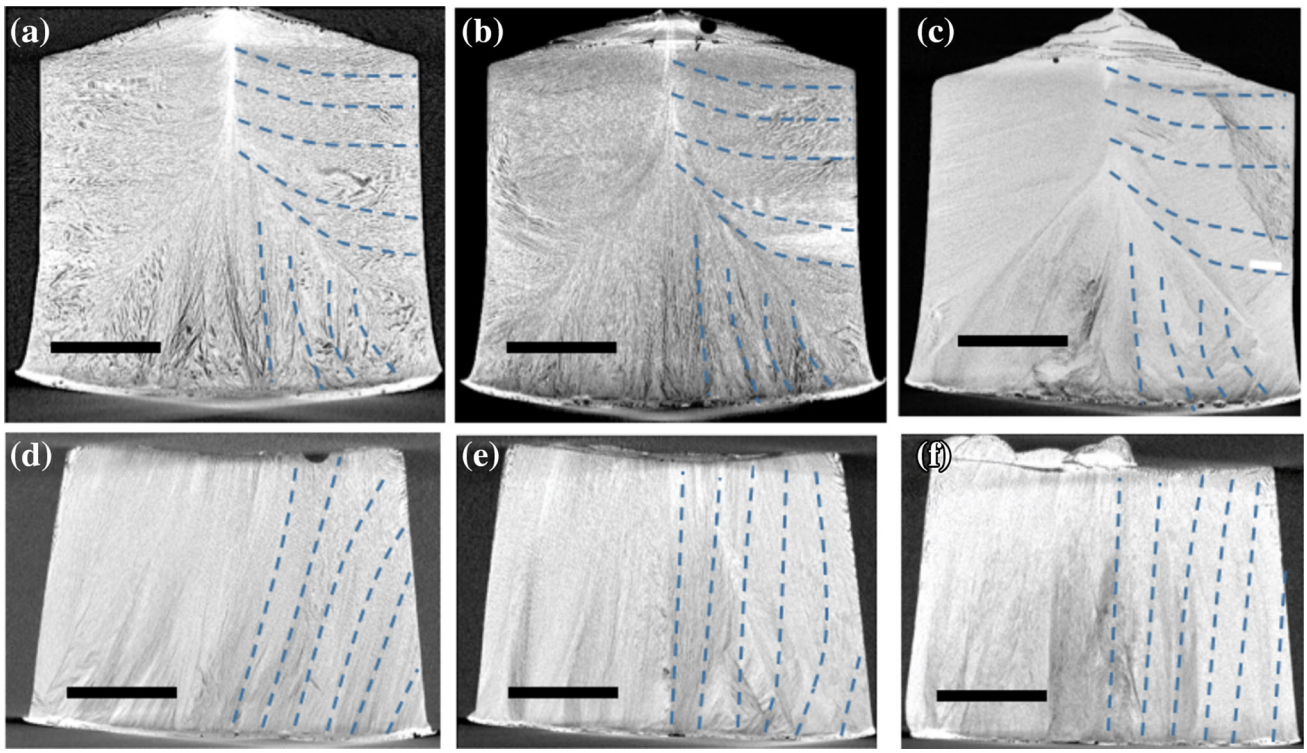

Fig. 3. Micro-CT images of the freeze-cast samples manufactured using the aluminum mold at cooling temperatures of: (a) 203 K, (b) 143 K and (c) 103 K. Corresponding freeze-cast samples manufactured using the rubber mold are shown for cooling temperatures of: (d) 203 K, (e) 143 K and (f) 103 K. The blue dashed lines show aligned porosity orientations. The scale bar in each figure represents 10 mm. Both aluminum and rubber mold dimensions are 40 mm inner diameter, 50 mm height and 5 mm wall thickness.

does not cause a substantial change in temperature difference. Moreover, as shown in Fig. 5b, the mold can also be tuned to control the slurry temperature differences through adjustment of the mold diameter. As the diameter of the mold is reduced from approximately 60 mm, a more even cooling distribution is obtained as shown in Fig. 5b. In general, the mold design can be tuned to achieve a particular cooling pattern and microstructural texture.

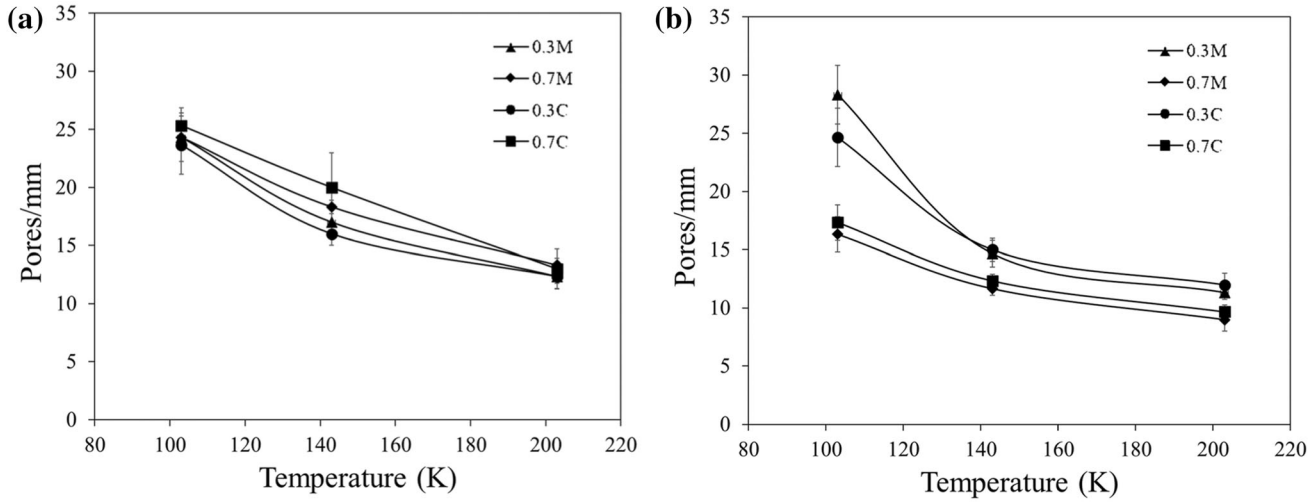

Fig. 4. Measured variation of pore density (pores/mm) as a function of freezing temperature for different positions within the freeze-cast samples. (a) Aluminum mold; (b) rubber mold.

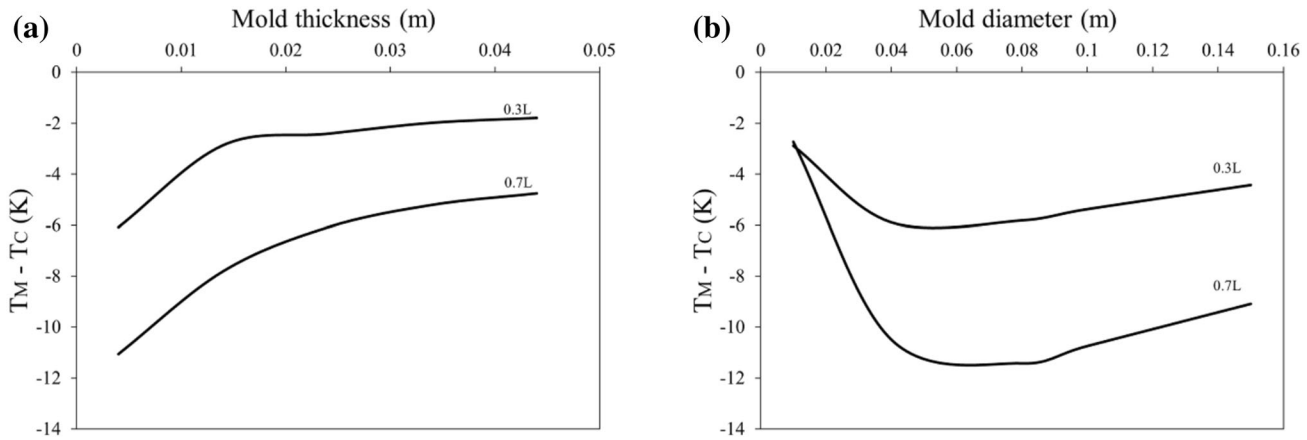

Fig. 5. Effect of mold geometry on temperature differences calculated using the FEA. (a) Mold thickness; b) mold internal diameter.

Figure 6 shows the effects of the thermal parameters on the temperature differences at the points of interest based on the FEM. Specifically, the importance of the freezing temperature, convective coefficient and thermal conductivity is shown in Fig. 6a–c, respectively. As shown in Fig. 6a, the freezing temperature is shown to have a linear effect on the temperature difference between the points of interest, and as the freezing temperature increases more uniform cooling patterns are obtained. External variables can also have an effect on the cooling patterns. For instance, the air speed around the mold, which is represented by the convective coefficient, has an important effect on temperature differences as shown in Fig. 6b. A higher convective coefficient promotes larger differences in temperature (Fig. 6b). This parameter is easy to adjust in the manufacturing process to control the morphology of pores in the sample. On the other hand, Fig. 6c shows the effect of the mold thermal conductivity between 1 W/m K^{-1} (i.e., rubber) and 167 W/m K^{-1} (i.e., aluminum) on the temperature difference between the points of interest. As shown by the response, the thermal conductivity of the mold material directly influences the cooling patterns obtained. That is also apparent from the solidification patterns in Fig. 3. Molds with higher thermal conductivities promote faster freezing of the slurry near the mold wall than at the center (Fig. 3a–c). Furthermore, for a thermal conductivity of approximately 5 W/m K^{-1}, the difference in temperature between the two points is a minimum, which results in an even cooling pattern and leads to a horizontal temperature gradient.

Figure 7 shows the temperature distributions in the mold as a function of the freezing temperature using both rubber and aluminum molds. Results for the aluminum mold and the rubber mold are shown

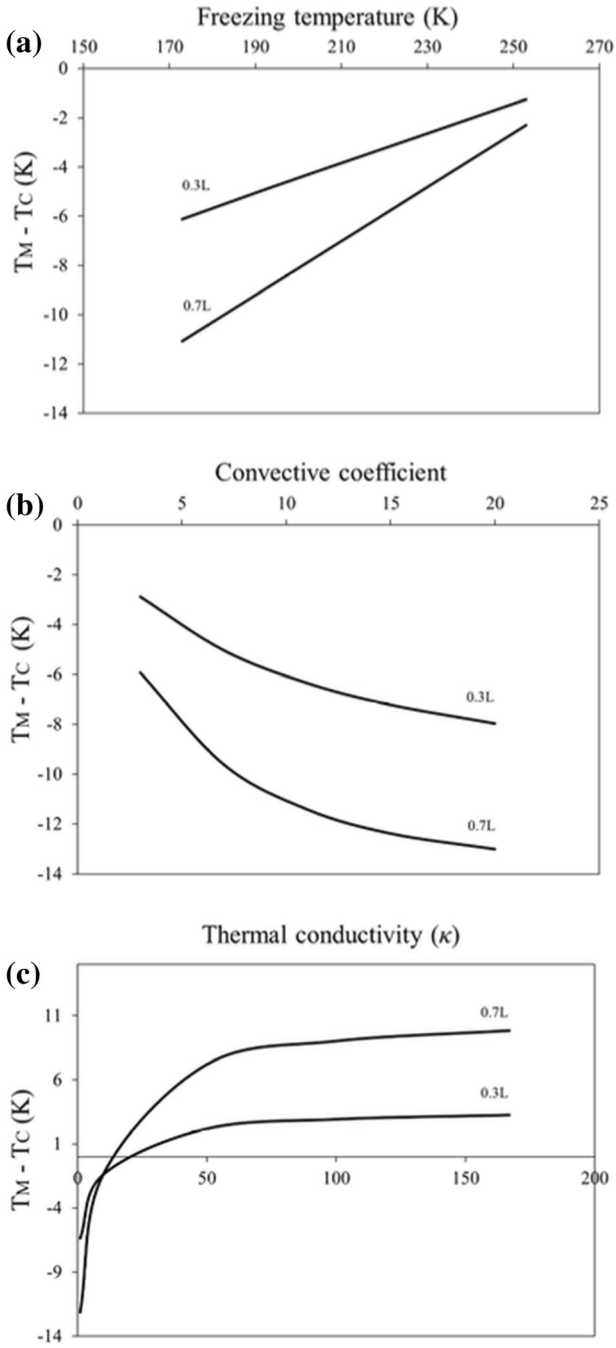

Fig. 6. Effect of thermal variables on temperature differences as calculated using the FEA. (a) Freezing temperature; (b) convective coefficient; (c) thermal conductivity.

at three different temperatures (203 K, 143 K and 93 K) in Fig. 7a–c and d–f, respectively. There are clear differences in the cooling patterns within the experimental domains for each mold material. For a given mold material, the cooling gradients have the same orientation with respect to the freezing direction. Nevertheless, the differences in the temperature range with freezing temperatures are significant.

Solidification is a critical stage in the freeze-casting process since the crystal morphology determines the resulting pore characteristics. While there are different crystal structures that can be formed with water-based slurries,[39] hexagonal ice crystals are the most common.[9] During the phase transition of liquid water to ice, the disordered liquid molecules become organized via hydrogen bonding on a process that can be divided into nucleation and crystal growth, both having an impact on the crystals formed.[40] During nucleation, water molecules are initially organized to form the solid that will undergo growth to form the crystals. The nucleation process is primarily stochastic and cannot be completely controlled.[41,42] Once it has occurred, the newly formed nuclei undergo a process called secondary nucleation, which leads to the development of new crystals.[43,44] After this initial nucleation, the remaining liquid undergoes crystal growth.[45]

There are two preferential axes of crystal growth, including the *a* and *c* axes, with the *c-axis* growing 10^{-2}–10^{-3} slower than the *a-axis*.[39] The *a-axis* is parallel to the temperature gradient, establishing the orientation of the main crystals in such directions, while the *c-axis* crystal growth is perpendicular to the temperature gradients, promoting interconnectivity between crystals and resulting in pore interconnectivity in the final cast material (Fig. 8).

The mechanisms driving crystal growth explain why there are no significant differences in pore density as a function of position in the freeze castings produced using the aluminum mold. With this mold the temperature tends to be homogenized close to the walls because of its high thermal conductivity. On the other hand, higher temperature gradients were found at 0.3 L and 0.7 L with the rubber mold because of its thermal insulating nature. Therefore, if there is a large mismatch between the thermal properties of the ceramic slurry and mold, horizontal temperature gradients will develop, affecting the growth kinetics of the crystals and the pore characteristics of the material obtained. Thus, the temperature gradients and their orientation can be chosen to develop a desired pore structure. Figure 8 shows the influence of temperature gradients on the pore orientation. Note that the freeze casting shows pore orientations that depend on the specific thermal properties of the mold material and the position analyzed. The orientation of the pores is governed by–and aligned with—the temperature gradients as indicated by the arrows in the figure. Thus, when a complex pore morphology is to be produced by freeze casting, the temperature gradients have to be considered in the mold design.

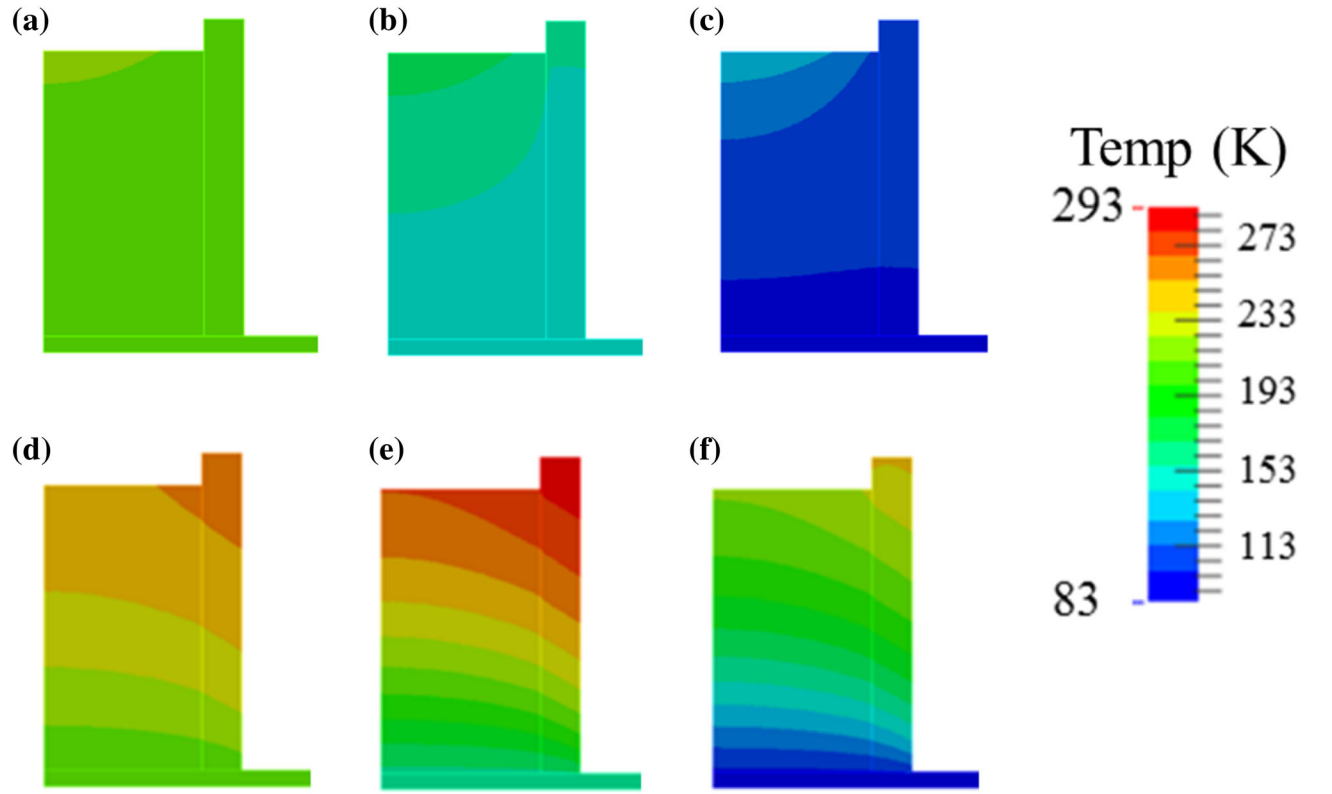

Fig. 7. Calculated temperature differences with varying molds and freezing temperatures. Aluminum mold: (a) 203 K; (b) 143 K; (c) 93 K. Rubber mold: (d) 203 K; (e) 143 K; (f) 93 K.

The variables affecting the cooling patterns within freeze castings have been described, as well as how specific mold and thermal variables affect the cooling patterns within the slurry domain, and their effect on the pore morphology has been shown. Alumina was used in this study as a material with known properties and characteristics. Different parameters such as the zeta potential, thermal properties, sedimentation, particle size and morphology must be considered if a different material is going to be used. However, if these parameters are correctly controlled in the slurry and the numerical model includes the main thermal parameters and dimensional conditions of the mold used, it is expected that the temperature gradients can be correctly predicted and hence the final pore morphology of the part fabricated. Results of the current work can help to guide the mold design and the thermal conditions necessary to achieve a desired pore morphology. It is worth noting that if more details are required for prediction, a more elaborate multiphasic model including the dynamics of crystal growth and changes in volume has to be developed. Nonetheless, a simple model like the one presented here can lead to a realistic control of the porosity orientation in freeze-cast materials and can be used to manufacture bioinspired porous materials.

CONCLUSION

A combined experimental and numerical study was conducted to characterize the cooling patterns obtained during solidification in freeze casting and contributions from the primary process parameters. It was found that the freezing pattern and cast microstructure are strongly dependent on the mold design and temperature gradient, which affect the pore morphology of the cast material. Temperature gradients within the mold domain are controlled by the sample volume, shape, freezing rate, convective coefficient, and mold material and geometry. Finite element modeling served as a tool to understand the temperature gradients quantitatively and their contribution to the pore morphology. A porous structure with the required morphology can be obtained via tuning of the temperature gradients during freezing of the slurry through careful control of the dimensional and thermal properties of the mold.

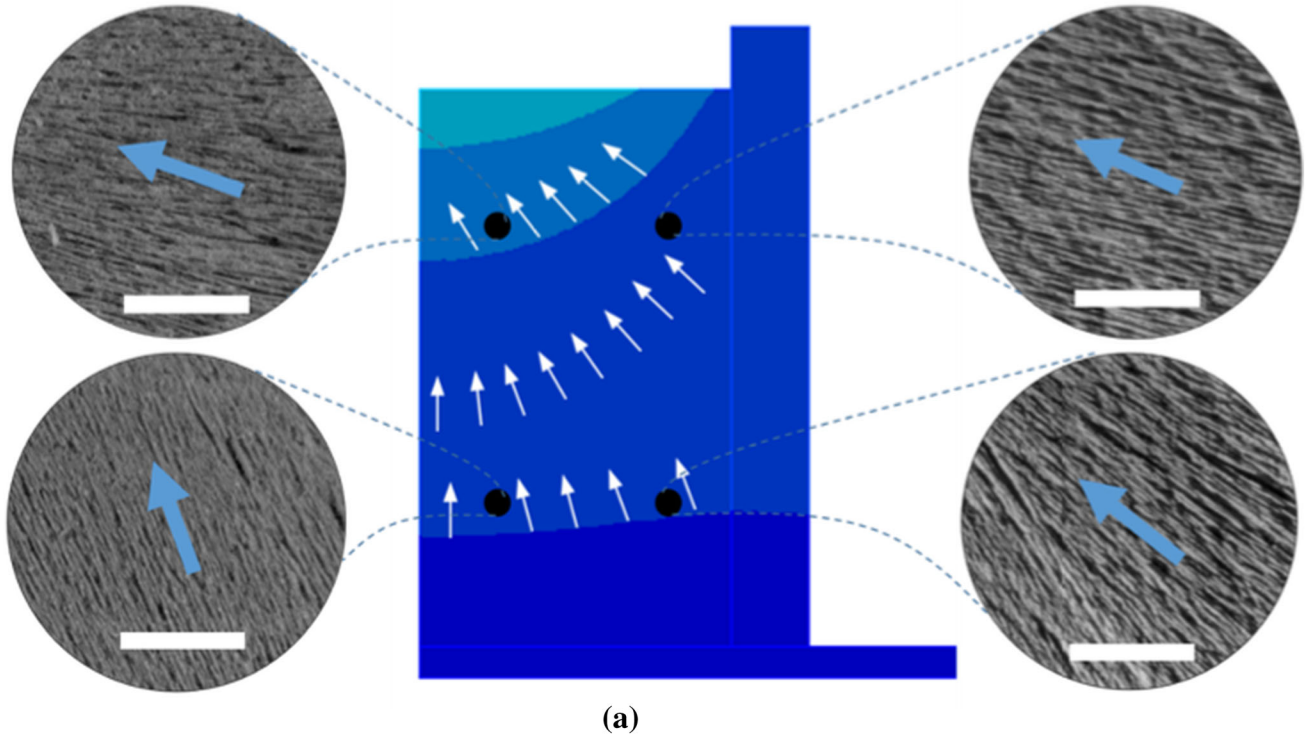

(a)

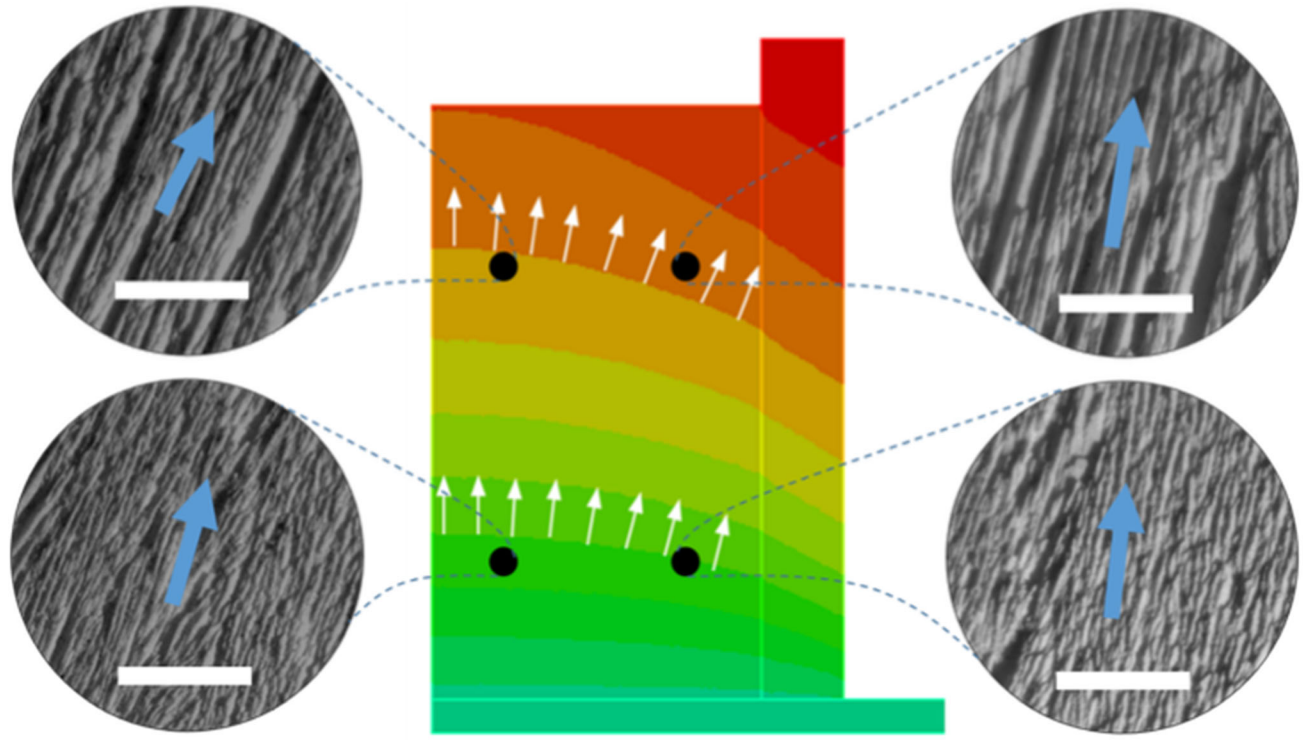

(b)

Fig. 8. Relation between temperature gradients and pore orientation for (a) aluminum mold with freezing temperature of 93 K. (b) Rubber mold with freezing temperature of 143 K. The arrows show the direction of the temperature gradient and *a-axis* of crystal growth. The scale bar represents 1 mm.

ACKNOWLEDGEMENTS

The authors express their gratitude to Universidad EAFIT and Departamento Administrativo de Ciencia Tecnología e Innovación, Colciencias, for Contract 0210-2013 for their financial support.

ELECTRONIC SUPPLEMENTARY MATERIAL

The online version of this article (https://doi.org/10.1007/s11837-019-03974-y) contains supplementary material, which is available to authorized users.

REFERENCES

1. J.D. Currey, *Bones: Structure and Mechanics* (Princeton NJ: Princeton University Press, 2002).
2. M.A. Meyers, P.Y. Chen, A.Y.M. Lin, and Y. Seki, *Progress Mater. Sci.* 53, 1 (2008).
3. N. Reznikov, R. Shahar, and S. Weiner, *Acta Biomater.* 10, 3815 (2014).
4. A. Sellinger, P.M. Weiss, A. Nguyen, Y.F. Lu, R.A. Assink, and W.L. Gong, *Nature* 394, 256 (1998).
5. Z. Tang, N.A. Kotov, S. Magonov, and B. Ozturk, *Nat. Mater.* 2, 413 (2003).
6. H. Seitz, W. Rieder, S. Irsen, B. Leukers, and C. Tille, *J. Biomed. Mater. Res. Part B Appl. Biomater.* 74, 782 (2005).
7. Q. Fu, E. Saiz, and A.P. Tomsia, *Adv. Funct. Mater.* 21, 1058 (2011).
8. W.L. Li, K. Lu, and J.Y. Walz, *Int. Mater. Rev.* 57, 37 (2012).
9. S. Deville, *Adv. Eng. Mater.* 10, 155 (2008).
10. M.C. Gutiérrez, M.L. Ferrer, and F. del Monte, *Chem. Mater.* 20, 634 (2008).
11. L. Qian and H.F. Zhang, *J Chem. Technol. Biotechnol.* 86, 172 (2011).
12. S. Gil-Durán and E.A. Ossa, *Ingeniería y competitividad* 18, 133 (2016).
13. L.S. Kristen and C.D. David, Progress. *Mater. Sci.* 94, 243 (2018).
14. S.W. Sofie and F. Dogan, *J. Am. Ceram. Soc.* 84, 1459 (2001).
15. C.M. Pekor, P. Kisa, and I.J. Nettleship, *Am. Ceram. Soc.* 91, 3185 (2008).
16. C. Peko, B. Groth, and I.J. Nettleship, *Am. Ceram. Soc.* 93, 115 (2010).
17. S. Deville and G. Bernard-Granger, *J. Eur. Ceram. Soc.* 112, 121 (2010).
18. Y. Tang, K. Zhao, L. Hu, and Z. Wu, *Ceram. Int.* 39, 9703 (2013).
19. S. Flauder, T. Heinze, and F.A. Müller, *Cellulose* 21, 97 (2014).
20. G.K. Ulrike, M.S. Wegst, E.D. Amalie, and M.H. Philipp, *Phil. Trans. R. Soc. A.* 368, 2099 (2010).
21. E.C. Hammel, O.R. Ighodaro, and O.I. Okoli, *Ceram. Int.* 40, 15351 (2014).
22. R. Liu, T. Xu, and C. Wang, *A. Ceram. Int.* 42, 2907 (2016).
23. K. Shanmugam, T.K. Radhakrishnan, and P. Kalaichelvi, *Cryst. Growth Des.* 16, 6663 (2016).
24. M.E. Launey, E. Munch, D.H. Alsem, H.B. Barth, E. Saiz, A.P. Tomsia, and R.O. Ritchie, *Acta Mater.* 57, 2919 (2009).
25. S. Deville, *Freezing Colloids: Observations, Principles, Control, and Use* (Cham: Springer, 2017), pp. 1–46.
26. K.L. Scotti and D.C. Dunand, *Prog. Mater Sci.* 94, 243 (2018).
27. S. Algharaibeh, A.J. Ireland, and B. Su, *J. Eur. Ceram. Soc* 39, 514 (2019).
28. K.M. Pawelec, A. Husmann, S.M. Best, and R.E.J. Cameron, *Mater. Sci.* 50, 7537 (2015).
29. N. Wang, Y. Liu, Y. Zhang, Y. Du, and J. Zhang, *Ceram. Int.* 45, 11558 (2019).
30. A. Husmann, K. Pawelec, C. Burdett, S. Best, and R. Cameron, *Genesis* 6, 8 (2015).
31. A. Rouhollahi, O. Ilegbusi, S. Florczyk, K. Xu, H. Foroosh. Ann Biomed Eng, 1–13 (2019).
32. C.B. Carter and M.G. Norton, *Ceramic Materials: Science & Engineering*, 2nd ed. (Berlin: Springer, 2013).
33. S. Biggs and T.W. Healy, *J. Chem. Soc. Faraday Trans.* 90, 3415 (1994).
34. A. Preiss, B. Su, S. Collins, and D. Simpson, *D. J. Eur. Ceram. Soc.* 32, 1575 (2012).
35. R.W. Lewis, K. Morgan, H.R. Thomas, and K.N. Seetharamu, *The finite element method in heat transfer analysis* (Hoboken: Wiley, 1996).
36. X.Q. Wang and A.S. Mujumdar, *Int. J. Thermal Sci.* 46, 1 (2007).
37. J.C. Maxwell, *A Treatise on Electricity and Magnetism*, 2nd ed. (Oxford: Clarendon Press, 1881).
38. Y. Xuan and W. Roetzel, *Int. J. Heat Mass Transfer* 43, 3701 (2000).
39. W.J. Boettinger, S.R. Coriell, A.L. Greer, A. Karma, W. Kurz, M. Rappaz, and R. Trivedi, *Acta Mater.* 48, 43 (2000).
40. P.V. Hobbs, *Ice Physics* (Oxford: Oxford University Press, 2010).
41. M. Matsumoto, S. Saito, and I. Ohmine, *Nature* 416, 409 (2002).
42. V. Ayel, O. Lottin, M. Faucheux, D. Sallier, and H. Peerhossaini, *Int. J. Heat Mass Transfer.* 49, 2006 (1876).
43. A. Myerson, *Handbook of Industrial Crystallization* (Oxford: Butterworth-Heinemann, 2002).
44. M.C. Flemings, *Metall Trans* 5, 2121–2134 (1974).
45. L. Rey and J.C. May, *Freeze-Drying/Lyophilization of Pharmaceutical & Biological Products* (Boca Raton: CRC Press, 2004).